The Journal of the Korean Society of
Coastal and Ocean Engineers
Vol. 6, No. 1, pp. 1~11, March 1994

Wind-Driven Circulation Using a Curvilinear Hydrodynamic Three-Dimensional Model
曲線形格子 三次元 數値模型을 利用한 바람에 의한 물의 循環

Hye Keun Lee*
李 慧 根*

Abstract □ A curvilinear hydrodynamic three-dimensional model is presented for the study of wind-driven circulation in a shallow lake. Numerical results are compared with field data. Thermal stratification effects were found to be critical to the successful simulation of circulation under increasing winds. When there are insufficient meteorological data, the so-called inverse method can be used for the estimation of heat flux.

要 旨 : 곡선형격자 삼차원 수치모델이 소개되며 바람에 의한 물의 순환을 계산하기 위하여 얕은 호수에서 적용되었다. 수치모델의 결과가 실측자료와 비교되었으며, 바람이 점차 증가할 때 물의 성층에 의한 효과가 좋은 계산 결과를 얻기 위하여 결정적임을 알 수 있었다. 기상자료가 불충분할 때 소위 Inverse Method가 물 표면에서 열흐름을 추정하기 위하여 사용되었다.

1. INTRODUCTION

Estuaries and lakes are valuable resources for a variety of human needs: drinking water, agricultural use, navigation, waste water disposal, recreation sites, cooling reservoirs for power plants, etc. On the other hand, estuaries and lakes can be dangerous to people under certain circumstances such as during flooding and the deterioration of water quality due to the excessive loading of contaminants into the lake. Water movement in estuaries and lakes is driven by tide, wind, density gradient, waves, and tributary flow, but it is primarily influenced by wind action.

Water quality is of utmost importance. So long as human activities are limited to a small part of a lake, it may appear that the lake has an unlimited capacity of self-purification. However, as population and human development increase, a lake may not be able to endure the excessive stresses caused by human actions, and water quality may become deteriorated. Typical evidence of poor water quality includes sudden algal bloom, colored water, fishkill, taste and odor in drinking water, and floating debris of plants. Eutrophication is the process in which excessive loading of nutrients, organic matter, and sediments into lakes results in an increase of primary production. Sources of eutrophication are increased use of fertilizer, waste water discharge, and precipitation of polluted air.

Numerical models are valuable tools for simulating and understanding water movement in lakes. Once a rigorously developed model is calibrated with measured data, it can be used to estimate the flow near a man-made structure or to predict the movement of contaminants including oil spill, sediments, etc. During the 1970s and 1980s, vertically averaged two-dimensional numerical models, which can compute only the depth average currents and surface elevations, were widely used because they are simple and need little computer time. However, since they could not give accurate results for cases

*플로리다大學 海岸·海洋工學科(Coastal and Oceanographic Engineering Department, University of Florida, Gainsville, FL 32611, USA)

where the vertical distributions of currents and temperature are required, three-dimensional models are required.

Numerical modeling requires the discretization of the computation domain. Past numerical models which were developed during 1970s generally used a rectangular grid. However, to represent the complex geometry such as the shoreline and the boundary between the vegetation zone and the open water in Lake Okeechobee, a very fine rectangular grid is required. On the other hand, boundary-fitted grids can be and have been used in recent models to represent the complex geometry with a relatively smaller number of grid points.

2. GOVERNING EQUATIONS

The basic equations which govern the water circulation in lakes, reservoirs, and estuaries, are presented. Because the details can be found in other references (e.g., Sheng, 1986; Sheng, 1987), the governing equations are presented here without detailed derivations.

The equations which govern the water motion in the water bodies consist of the conservation of mass and momentum, the conservation of heat and salinity, and the equation of state. Because Lake Okeechobee is a fresh water lake, the salinity equation is not considered. The following assumptions are used in the Curvilinear Hydrodynamic 3-Dimensional Model (CH3D).

(1) Reynolds averaging: Three components of velocity, pressure, and temperature are decomposed into mean and fluctuating and time-averaged components.

(2) Hydrostatic assumption: Vertical length scale in lakes is small compared to the horizontal length scale, and the vertical acceleration is small compared with the gravitational acceleration.

(3) Eddy viscosity concept: After time-averaging, the second-order correlation terms in the momentum equation are turbulence stresses, which are related to the product of eddy viscosity and the gradient of mean strain.

(4) Boussinesq approximation: Density variation of water is small, and variable density is considered only in the buoyancy term.

2.1 Generation of Numerical Grid

2.1.1 Cartesian Grid

In order to solve numerically the governing equations, finite difference approximations are introduced to the original governing equations, and solutions are obtained at discrete points within the domain. Therefore, a physical domain of interest must be discretized. When a simple physical domain is considered, Cartesian grid can be used and hence grid generation and development of finite-difference equations are relatively easy.

Unfortunately, most physical domains in lakes or estuaries are complex. This method has such disadvantages as inaccuracies at boundaries or complications of programming due to unequal grid spacing near boundaries.

2.1.2 Curvilinear Grid

In order to resolve better the complex geometries in the physical domain, boundary-fitted (curvilinear) grid can be used. In general, acurvilinear grid can be obtained by use of (1) algebraic methods, (2) conformal mapping, and (3) numerical grid generation.

Algebraic grid generation uses an interpolation scheme between the specified boundary points to generate the interior grid points. This is simple and fast computationally, while the smoothness and skewness are hard to control. Conformal mapping method is based on complex variables, so the determination of mapping function is a difficult task. Many practical applications rely on numerical grid generation techniques.

2.1.3 Numerical Grid Generation

Partial differential equations are solved to obtain the interior grid points with specified boundary points. Thompson (1983) developed an elliptic grid generation code (WESCORA) to generate a two-dimensional, boundary-fitted grid in a complex domain.

To help understand the physical reasoning of this method, consider a rectangular domain. When the temperature is specified along the horizontal boundary, then the temperature distribution inside can be obtained by solving the heat equation. Therefore, isothermal lines can be drawn. Also, other isother-

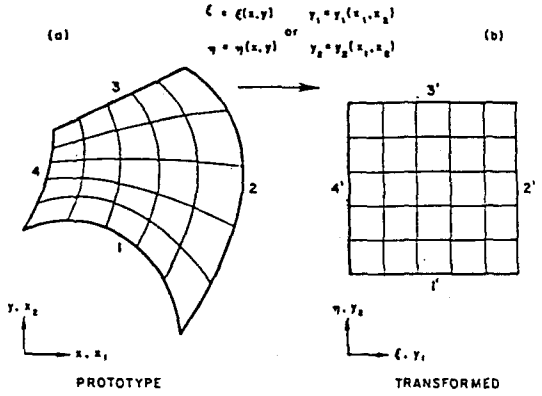

Fig. 1. A computational domain and a tranformed coordinate system.

mal lines can be obtained with the specified temperature in the vertical direction. By superimposing these isothermal lines, intersection points of isothermal lines can be considered as grid points.

WESCORA solves Poisson equations with the same idea in a complex domain. Consider the following set of equations (see Figure 1):

$$\xi_{xx}+\xi_{yy}=P \tag{1}$$

$$\eta_{xx}+\eta_{yy}=Q \tag{2}$$

with the follwoing boundary conditions:

$$\xi=\xi(x, y) \quad \text{on 1 and 3}$$
$$\eta=\text{constant} \tag{3}$$

$$\xi=\text{constant} \quad \text{on 2 and 4}$$
$$\eta=\eta(x, y) \tag{4}$$

where the functions P and Q may be chosen to obtain the desired grid resolution and alignment.

In practice, one actually solves the following equations which are readily obtained by interchanging the dependent and independent variables in Eqs. (1) and (2):

$$\alpha x_{\xi\xi}-2\beta x_{\xi\eta}+\gamma x_{\eta\eta}+\alpha\bar{P}x_{\xi}+\gamma\bar{Q}x_{\eta}=0 \tag{5}$$

$$\alpha y_{\xi\xi}-2\beta y_{\xi\eta}+\gamma y_{\eta\eta}+\alpha\bar{P}y_{\xi}+\gamma\bar{Q}y_{\eta}=0 \tag{6}$$

where

$$\alpha=x_{\eta}^2+y_{\eta}^2$$
$$\beta=x_{\xi}x_{\eta}+y_{\xi}y_{\eta}$$
$$\gamma=x_{\xi}^2+y_{\xi}^2$$

$$P=\frac{1}{J^2}(x_{\eta}^2+y_{\eta}^2)\bar{P}$$

$$Q=\frac{1}{J^2}(x_{\xi}^2+y_{\xi}^2)\bar{Q}$$

$$J=x_{\xi}y_{\eta}-x_{\eta}y_{\xi} \tag{7}$$

with the transformed boundary conditions:

$$x=f_i(\xi, \eta_i) \quad \text{on i=1 and 3}$$
$$y=g_i(\xi, \eta_i) \tag{8}$$

$$x=f_i(\xi_i, \eta) \quad \text{on i=2 and 4}$$
$$y=g_i(\xi_i, \eta) \tag{9}$$

2.1.4 Transformation Rules

Generation of a boundary-fitted grid is an essential step in the development of a boundary-fitted hydrodynamic model. It is, however, only the first step. A more important step is the transformation of governing equations into the boundary-fitted coordinates. A straightforward method is to transform only the independent variables, i.e., the coordinates, while retaining the Cartesian components of velocities. Johnson (1982) developed such a 2-D vertically-integrated model of estuarine hydrodynamics. The advantage of the method is its simplicity in generating the transformed equations via chain rule. The dimensional forms of the continuity equation and the vertically-integrated momentum equations are shown by Eqs. (20) and (21) in Appendix A of Sheng (1986). The resulting equations, however, are rather complex. Even when an orthogonal or a conformal grid is used, the equations do not become any simpler. Additional disadvantages are that (1) the boundary conditions are quite complicated because the Cartesian velocity components are generally not aligned with the grid lines, (2) the staggered grid cannot be readily used, and (3) numerical instability may develop unless additional variables (e.g., surface elevation or pressure) are solved at additional grid points (Sheng, 1986).

To alleviate the problems mentioned in the previous paragraph, Sheng (1986) chose to transform the dependent variables as well as the independent variables. Equations in the transformed coordinates (ξ, η) can be obtained in terms of the contravariant, or covariant, or physical velocity components via tensor transformation (e.g., Sokolnikoff, 1960). As

shown in Fig. 8 of Appendix A of Sheng (1986), the contravariant components (u^i) and physical components $u(i)$ of the velocity vector in the non-Cartesian system are locally parallel or orthogonal to the grid lines, while the covariant components (u_i) are generally not parallel or orthogonal to the local grid lines. The three components are identical in a Cartesian coordinate system. The following relationships are valid for the three components in a non-Cartesian system:

$$u^i=(g_{ii})^{-1/2}u(i) \qquad \text{(no sum on i)} \qquad (10)$$

$$u_i=(g_{ii})^{-1/2}g_{ij}u(j) \qquad \text{(no sum on i)} \qquad (11)$$

$$u(i)\equiv\tilde{u}_i \qquad (12)$$

where g is the diagonal element of the metric tensor g_{ij}:

$$g_{ij}=\frac{\partial x^l}{\partial\xi^i}\frac{\partial x^n}{\partial\xi^j}\delta_{ln} \qquad (13)$$

which for the two-dimensional case of interest is

$$g_{ij}=\begin{pmatrix} x_\xi^2+y_\xi^2 & x_\xi x_\eta+y_\xi y_\eta \\ x_\eta x_\xi+y_\eta y_\xi & x_\eta^2+y_\eta^2 \end{pmatrix}=\begin{pmatrix} g_{11} & g_{12} \\ g_{21} & g_{22} \end{pmatrix} \qquad (14)$$

The three components follow different rules for transformation between the prototype and the transformed plane:

$$\bar{u}^i=\frac{\partial\xi^i}{\partial x^j}u^j \qquad (15)$$

$$\bar{u}_i=\frac{\partial\xi^j}{\partial x^i}u_j \qquad (16)$$

$$\bar{u}(i)=(\bar{g}_{ii})^{1/2}\frac{\partial\xi^i}{\partial x^j}u(i) \qquad (17)$$

where the unbarred quantities represent the components in the prototype system, while the barred quantities represent the components in the transformed system.

2.2 Tensor-Invariant Governing Equations

Before transforming the governing equations, it is essential to write them first in tensor-invariant forms, i.e., equations which are independent of coordinate translation and rotation. For simplicity, unbarred quantities are used to denote the variables in the transformed system unless otherwise indicated.

Following the rules described in the previous paragraph, the following equations are obtained (Sheng, 1986):

$$\zeta+\frac{\beta}{\sqrt{g_o}}\frac{\partial}{\partial x^k}(\sqrt{g_o}Hu^k)=0 \qquad (18)$$

$$\begin{aligned}\frac{1}{H}\frac{\partial Hu^k}{\partial t}=&-\zeta!^k-g_{nj}\varepsilon^{kj}u^n\\&-\frac{Ro}{H}\left[(Hu^iu^k)_{,i}+\frac{\partial hu^k\omega}{\partial\sigma}\right]\\&+\frac{E_v}{H^2}\frac{\partial}{\partial\sigma}\left(A_v\frac{\partial u^k}{\partial\sigma}\right)+E_HA_Hu^k{}_{,m}!^m\\&-\frac{Ro}{Fr_D^2}\left[H\int_\sigma^0\rho!^k d\sigma+\mathrm{H}!^k\left(\int_\sigma^0\rho d\sigma+\sigma\rho\right)\right]\end{aligned} \qquad (19)$$

where $\partial/\partial x_k$ is the partial derivative, g_{ln} is the metric tensor while $g_o\equiv J=x_\xi y_\eta-x_\eta y_\xi$ is the determinant of the metric tensor, u^k is the contravariant velocity, $(\ )_{,i}$ represents the covariant spatial derivative, $!^k$ represents the contravariant spatial derivative, ε^{kj} is the permutation tensor and

$$\varepsilon^{12}=-\frac{1}{\sqrt{g_o}}$$

$$\varepsilon^{21}=\frac{1}{\sqrt{g_o}}$$

$$\varepsilon^{11}=\varepsilon^{22}=0 \qquad (20)$$

The covariant and contravariant differentiations are defined by

$$u^i{}_{,j}=u^i{}_{:j}+D^i_{\alpha j}u^\alpha \qquad (21)$$

$$S!^k=g^{km}S_{,m} \qquad (22)$$

where: j represents partial differentiation and D^i_{ij} represents the Christoffel symbol of the second kind:

$$D^i_{jk}=g^{in}D_{njk} \qquad (23)$$

where g^{in} represents the inverse metric tensor, h_{in}, and D_{njk} is the Christoffel symbol of the first kind:

$$D_{ijk}=\frac{1}{2}(g_{ij:k}+g_{ik:j}-g_{jk:i}) \qquad (24)$$

2.3 Dimensionless Equations in Boundary-Fitted Grids

$$\zeta+\frac{\beta}{\sqrt{g_o}}\left[\frac{\partial}{\partial\xi}(\sqrt{g_o}Hu)+\frac{\partial}{\partial\eta}(\sqrt{g_o}Hv)\right]=0 \tag{25}$$

$$\begin{aligned}\frac{1}{H}\frac{\partial Hu}{\partial t}=&-\left(g^{11}\frac{\partial\zeta}{\partial\xi}+g^{12}\frac{\partial\zeta}{\partial\eta}\right)+\frac{g_{12}}{\sqrt{g_o}}u+\frac{g_{22}}{\sqrt{g_o}}v\\&-\frac{Ro}{H}\left[\frac{\partial}{\partial\xi}(Huu)+\frac{\partial}{\partial\eta}(Huv)+(2D_{11}^{1}+D_{12}^{2})Huu\right.\\&\left.+(3D_{12}^{1}+D_{22}^{2})Huv+D_{22}^{1}Hvv+\frac{\partial Hu\omega}{\partial\sigma}\right]\\&+\frac{E_v}{H^2}\frac{\partial}{\partial\sigma}\left(A_v\frac{\partial u}{\partial\sigma}\right)\\&-\frac{Ro}{F_{r2}}\left[H\int_{\sigma}^{0}\left(g^{11}\frac{\partial\rho}{\partial\xi}+g^{12}\frac{\partial\rho}{\partial\eta}\right)d\sigma\right.\\&\left.+\left(g^{11}\frac{\partial H}{\partial\xi}+g^{12}\frac{\partial H}{\partial\eta}\right)\left(\int_{\sigma}^{0}\rho d\sigma+\sigma\rho\right)\right]\\&+E_HA_H\ \text{(Horizontal Diffusion)}\end{aligned} \tag{26}$$

$$\begin{aligned}\frac{1}{H}\frac{\partial Hv}{\partial t}=&-\left(g^{21}\frac{\partial\zeta}{\partial\xi}+g^{22}\frac{\partial\zeta}{\partial\eta}\right)-\left(\frac{g_{11}}{\sqrt{g_o}}u+\frac{g_{21}}{\sqrt{g_o}}v\right)\\&-\frac{Ro}{H}\left[\frac{\partial}{\partial\xi}(Huv)+\frac{\partial}{\partial\eta}(Hvv)+2D_{11}^{2}Huu\right.\\&\left.+(D_{11}^{1}+3D_{12}^{2})Huv+(D_{12}^{1}+2D_{22}^{2})Hvv\right]\\&+\frac{E_v}{H^2}\frac{\partial}{\partial\sigma}\left(A_v\frac{\partial v}{\partial\sigma}\right)\\&-\frac{Ro}{F_{r2}}\left[H\int_{\sigma}^{0}\left(g^{21}\frac{\partial\rho}{\partial\xi}+g^{22}\frac{\partial\rho}{\partial\eta}\right)d\sigma\right.\\&\left.+\left(g^{21}\frac{\partial H}{\partial\xi}+g^{22}\frac{\partial H}{\partial\eta}\right)\left(\int_{\sigma}^{0}\rho d\sigma+\sigma\rho\right)\right]\\&+E_HA_H\ \text{(Horizontal Diffusion)}\end{aligned} \tag{27}$$

where the horizontal diffusion terms are listed in Sheng (1986). The temperature equation can be obtained according to the same procedure as

$$\begin{aligned}\frac{1}{H}\frac{\partial HT}{\partial t}=&\frac{E_v}{Pr_v}\frac{\partial}{H^2\partial\sigma}\left(K_v\frac{\partial T}{\partial\sigma}\right)\\&-\frac{Ro}{H}\frac{1}{\sqrt{g_o}}\left[\frac{\partial}{\partial\xi}(\sqrt{g_o}HuT)+\frac{\partial}{\partial\eta}(\sqrt{g_o}HvT)\right]\\&-\frac{Ro}{H}\frac{\partial H\omega T}{\partial\sigma}+\frac{E_H}{Pr_H}\left[g^{11}T_{,1,1}+g^{12}T_{,1,2}\right.\\&\left.+g^{21}T_{,2,1}+g^{22}T_{,2,2}\right]\end{aligned} \tag{28}$$

2.4 Boundary Conditions and Initial Conditions

2.4.1 Vertical Boundary Conditions

The boundary conditions at the free surface ($\sigma=0$) are

$$\begin{aligned}&A_v\left(\frac{\partial u}{\partial\sigma},\ \frac{\partial v}{\partial\sigma}\right)=\frac{H}{E_v}(\tau_{s\xi},\ \tau_{s\eta})\\&\frac{\partial T}{\partial\sigma}=\frac{HPr_v}{E_v}\,q_s\end{aligned} \tag{29}$$

The boundary conditions at the bottom ($\sigma=-1$) are

$$\begin{aligned}&A_v\left(\frac{\partial u}{\partial\sigma},\ \frac{\partial v}{\partial\sigma}\right)=\frac{H}{E_v}(\tau_{b\xi},\ \tau_{b\eta})\\&\quad=\frac{U_r}{A_{vr}}H_rZ_rC_d\left[g_{11}u_1^2+2g_{12}u_1v_1+g_{22}v_1^2\right]^{1/2}(u_1,\ v_1)\\&\frac{\partial T}{\partial\sigma}=0\end{aligned} \tag{30}$$

where u_1 and v_1 are the contravariant velocity components at the first grid point above the bottom.

2.4.2 Lateral Boundary Conditions

Due to the use of contravariant velocity components, the lateral boundary conditions in the (ξ, η, σ) grid are similar to those in the (x, y, σ) system. Along the solid boundary, no-slip condition dictates that the tangential velocity is zero, while the slip condition requires that the normal velocity is zero. When flow is specified at the open boundary or river boundary, the normal velocity component is prescribed.

2.4.3 Initial Conditions

Initial conditions on vectors, if given in the Cartesian or prototype system, such as the velocity and the surface stress, must be first transformed before being used in the transformed equations. Thus, the surface stress in the transformed coordinate system is given by

$$\bar{\tau}^1=\frac{\partial\xi}{\partial x}\tau^1+\frac{\partial\xi}{\partial y}\tau^2 \tag{31}$$

$$\bar{\tau}^2=\frac{\partial\eta}{\partial x}\tau^1+\frac{\partial\eta}{\partial y}\tau^2 \tag{32}$$

where $\bar{\tau}^1$, $\bar{\tau}^2$ are the contravariant components of the stress in the transformed system and τ^1, τ^2 are the contravariant components in the Cartesian system. Note that in the Cartesian system, the contravariant, covariant, and physical components of a vector are identical. The contravariant components of the initial velocity vectors can be transformed in the same manner to obtain the proper initial

conditions for the transformed momentum equations.

2.4.4 Turbulence Parameterization

In this study, a simplified second-order closure model was used. Vegetation effects were parameterized by introducing an additional drag term in the form of a quadratic stress law (see Lee, 1993).

3. HEAT FLUX MODEL

All water bodies exchange heat with the atmosphere at air-sea interface. To estimate the net heat flux at the air-sea interface, it is necessary to consider seven processes: short-wave solar radiation, long-wave atmosphere radiation, reflection of solar radiation, reflection of atmospheric radiation, back radiation, evaporation, and conduction.

One way to estimate the net heat flux is to combine the seven complicated processes to an equation in terms of an equilibrium temperature and a heat exchange coefficient (Edinger and Geyer, 1967) as a boundary condition for the temperature equation as follows:

$$\rho_0 K_v \frac{\partial T}{\partial z} = q_s = K(T - T_e) \text{ at } z = \eta \tag{33}$$

where T_e, the equilibrium temperature, is defined as the water surface temperature at which there is no net heat exchange. This method will be called the "Equilibrium Temperature Method" to estimate the heat flux which includes the "Inverse Method" developed by Gaspar *et al.* (1990).

3.1 The "Inverse" Method

When there are insufficient meteorological data, the errors in the estimation of total heat flux at the air-sea interface can be large. To estimate better the total flux, the so-called inverse method (Gaspar *et al.*, 1990) was used in this study.

Total flux (q_t) can be divided into two parts: solar (q_{solar}) and nonsolar ($q_{nonsolar}$). While incoming solar radiation data are usually available, the nonsolar part is estimated by solving the vertical one-dimensional temperature equation coupled with the momentum equation.

3.1.1 Governing Equations

$$\frac{\partial T}{\partial t} = \frac{\partial}{\partial z}\left(K_v \frac{\partial T}{\partial z}\right) \tag{34}$$

$$\frac{\partial u}{\partial t} - fv = \frac{\partial}{\partial z}\left(A_v \frac{\partial u}{\partial z}\right) \tag{35}$$

$$\frac{\partial v}{\partial t} + fu = \frac{\partial}{\partial z}\left(A_v \frac{\partial v}{\partial z}\right) \tag{36}$$

3.1.2. Boundary Conditions

At the free surface

$$K_v \frac{\partial T}{\partial z} = \frac{q_t}{\rho} \tag{37}$$

$$A_v \frac{\partial u}{\partial z} = \frac{\tau_x}{\rho} \tag{38}$$

$$A_v \frac{\partial v}{\partial z} = \frac{\tau_y}{\rho} \tag{39}$$

where K_v is eddy diffusivity, A_v is eddy viscosity, q_t is the total heat flux, and τ_x and τ_y are wind stresses.

At the bottom

$$\frac{\partial T}{\partial z} = 0 \tag{40}$$

$$\tau_{bx} = \rho c_d \sqrt{u_1^2 + v_1^2}\, u_1 \tag{41}$$

$$\tau_{by} = \rho c_d \sqrt{u_1^2 + v_1^2}\, v_1 \tag{42}$$

where c_d is the drag coefficient and u_1 and v_1 are velocities at the lowest grid point above bottom.

Total flux q_t cannot be specified a priori because of unknown nonsolar flux, $q_{nonsolar}$. Therefore, a value of $q_{nonsolar}$ is first guessed and then corrected until the calculated and measured water temperatures are within an error limit. In this way, the total flux can be determined by summing up the solar and nonsolar parts. This total flux was later used as a boundary condition of temperature equation in the three-dimensional simulation.

4. MODEL APPLICATION TO LAKE OKEECHOBEE

4.1 Geometry

Lake Okeechobee, located between latitudes 27° 12′N and 26°40′N and longitudes 80°37′W and 81°

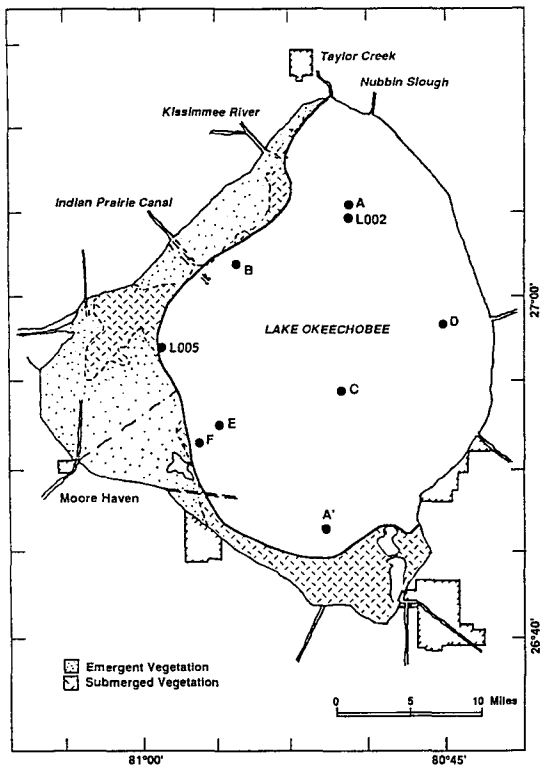

Fig. 2. Map of Lake Okeechobee.

08'W, is the largest freshwater lake in America, exclusive of the Great Lakes. With an average depth of approximately 3 m, and the deepest part less than 5 m deep, the basin is shaped like a very shallow saucer. The western part of the lake contains a great deal of emergent and submerged vegetation. According to satellite photos, marsh constitutes 24% of the lake surface area.

4.2 Some Recent Hydrodynamic Data

During the fall of 1988 and the spring of 1989, field data were collected by the Coastal and Oceanographic Engineering Department, University of Florida, U.S.A.

Six platforms were set up in Lake Okeechobee. Locations of the six platforms are shown in Figure 2. Measured data at these six platforms include wind, current, water temperature, wave and turbidity. In this study, wind data were used to compute the wind stress field, which is an essential boundary condition for the simulation of the wind-driven circulation. Current data were used to calibrate and validate the 3-D hydrodynamic model. The location and height of each of the current meters are shown in Table 1.

4.3 Tests of Model Performance

Comparing the simulated results with measured data is not a simple task. Two methods are used for the comparison. The first method is to plot simulated results and measured data. While this method can give a quick intuition, this can mislead the readers to the evaluation of the model's predictive ability because this method can show the model's ability qualitatively.

Therefore, quantitative measurements of the model's performance are necessary. Typical parameters are mean values of model and data, and the correlation coefficient between the model and data. A new parameter used here for the comparison is the index of agreement suggested by Willmott (1981) as follows:

$$d=1-\frac{\sum_{i=1}^{N}(P_i-O_i)^2}{\sum_{i=1}^{N}(|P_i'|+|O_i'|)^2} \tag{43}$$

where O_i is the observed value, P_i is the predicted value, $\overline{O}$ is the average of O_i, $\overline{P}$ is the average of P_i, $P'=P_i-\overline{O}$, and $O_i'=O_i-\overline{O}$. When the index of agreement is unity, predicted values perfectly agree with observed values in magnitude and sign.

4.4 Model Results

First a curvilinear grid was generated for the simulation as shown in Figure 3. Initially the model was run without thermal effect. For simplicity, results at Station C are presented.

4.5 Simulation of Currents without Thermal Stratification

Time series of wind stress at Station C show that the wind field is temporarily varying. Therefore, spatially and temporarily varying wind stress field was used for the simulation. Time series of the wind stress field shows that there is a significant diurnal variation of wind speed (Figure 4). Wind is calm early in the morning and strong in the afternoon and becomes calm again in the late night.

Table 1. Instrument mounting, spring deployment

Site	Arm	Current	Elev (cm)	Azim (deg)	Temp	Elev (cm)	Obs	Elev (cm)
A	Pressure Sensor 55695, Elev. 96 cm							
	Wind Sensor 5200, Water Depth 183 cm							
	1	80673	71	342	07	86	0076	86
B	Pressure Sensor 55696, Elev. 86 cm							
	Wind Sensor 5202, Water Depth 152 cm							
	1	80674	25	204	04	43	0078	43
	2	80675	114	181	02	132	0075	132
C	Pressure Sensor 48228, Elev. 297 cm							
	Wind Sensor 5203, Water Depth 366 cm							
	1	80679	61	330	01	79	0079	79
	2	80681	123	333	09	140	0077	140
	3	80680	284	342	06	302	0084	302
D	Pressure Sensor 55694, Elev. 254 cm							
	Wind Sensor 5200, Water Depth 335 cm							
	1	80672	79	270	08	79	0083	97
	2	80677	241	255	03	259	0082	259
E	Pressure Sensor 55699, Elev. 104 cm							
	Wind Sensor 5199, Water Depth 152 cm							
	1	80671	36	59	11	53	0081	53
	2	80678	116	72	05	135	0080	135
F	Pressure Sensor 55697, out of water							
	No Wind Sensor							
	1	80676	25	305	10	43	0085	43

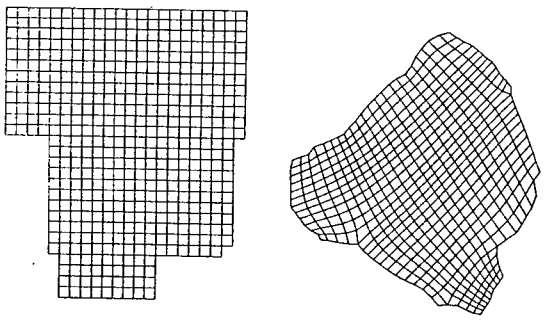

Fig. 3. Computation and physical domain of Lake Okeechobee.

The comparison of peak wind stress and peak current of field data shows that there is a time lag between the current and the wind, for example, Julian Day 150.8 in Figure 5. When the wind blows in the same direction over a considerable time period, water is piled up to create a set-up of surface elevation. Earlier studies indicated that it takes approximately one hour (Saville, 1952) for the current to respond to the wind. This is also manifested in the field data. The peak times of model currents compare quite well with the peak times of measured currents. When the wind changes direction or dies out, the wind set-up is released and the seiche starts to travel back and forth in the lake. Seiche period is computed by $T=2L/\sqrt{gh}$. When an average depth of 2.5 m and a length of 37 km, which is the length

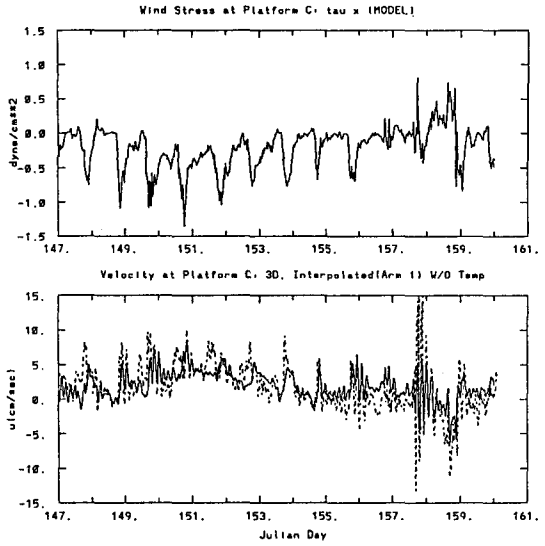

Fig. 4. Simulated (solid lines) and measured (dotted) currents (Arm 1: East-West direction).

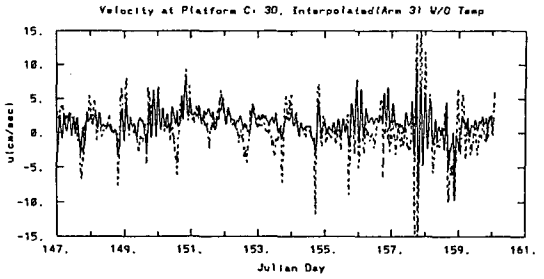

Fig. 5. Simulated (solid lines) and measured (dotted) currents (Arm 3: East-West direction).

Table 2. Index of agreement and RMS error at Station C

Arm	Index of Agreement		RMS Error	
	u	v	u(cm/sec)	v(cm/sec)
1	0.78	0.69	1.98	1.46
2	0.74	0.67	2.47	1.69
3	0.73	0.62	2.12	2.01

of lake excluding the marsh area in east-west direction, is used, the seiche period is about four hours. The model currents clearly show this period.

Currents at Station C are measured at Arms 1, 2 and 3, which are at the height of 17%, 33%, and 78% of the total depth above the bottom, respectively. It not easy to find out the corresponding model currents because the model uses σ stretching vertically. Therefore, the nearest layers are determined according to the percentage of total depth at the instrument heights. After that, linear interpolation between two layers is used for the model currents to be compared with field data. The long-term trend of time series of model current agrees well with that of field data. However, magnitudes of model currents (particularly the peak currents everyday) are generally smaller than those of field data. This can be explained with two possible reasons. First of all, the model currents are forced by 15-minute averaged wind data, while the measured currents are forced by the raw wind, which contains many "spikes" which are stronger than the 15-minute averaged wind. Thus, the simulated currents are expected to be less than the measured currents. Another possibility is due to some numerical dissipation which is always present in realistic simulations. The numerical dissipation can be reduced by using a smaller timestep.

Measured currents have another trend which the model could not simulate well. When the wind is mild, the measured currents are usually small. As the wind increases in the afternoon, the surface currents follow the wind direction. However, when the wind speed reduces, the setup is released and the currents change the direction. Therefore, general time history of measured currents have two peaks: a positive peak when the flow is from west to east during increasing easterly wind and a negative peak when the flow is from east to west during decreasing easterly wind.

While the model could simulate the positive peaks well, it missed many negative peaks as shown in Figure 5. As it will be shown later, the reason for this is that the model did not consider the thermal effect, and hence the eddy viscosity was not calculated correctly. A reduction of the time step did not lead to improved model results.

The index of agreement of this model simulation is shown in Table 2. The average index is 0.75 and 0.66 for the east-west currents and north-south currents, respectively.

4.6 Simulation of Currents with Thermal Stratification

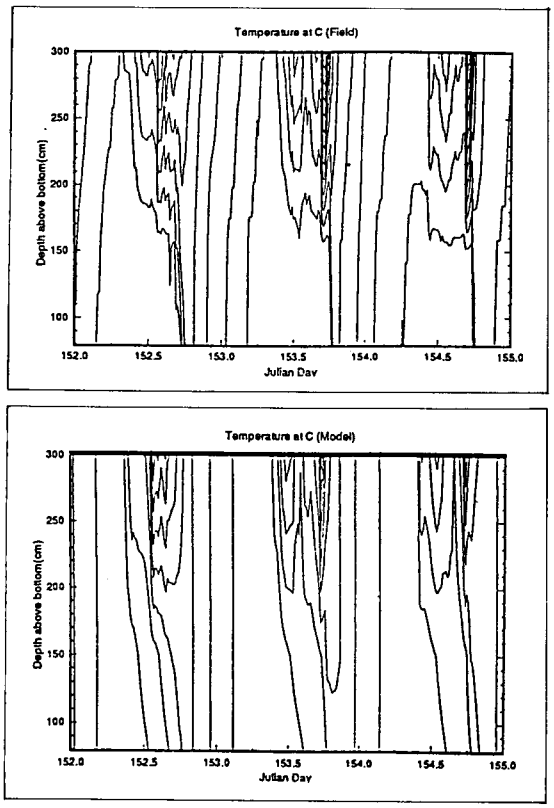

Fig. 6. Temperature contours of data and model at Station C between Julian days 152 and 155.

Table 3. Index of agreement and RMS error at Station C when thermal effect is considered

Arm	Index of Agreement		RMS Error	
	u	v	u(cm/sec)	v(cm/sec)
1	0.86	0.81	1.86	1.38
2	0.75	0.77	2.87	1.64
3	0.78	0.71	2.23	2.05

Initially, the model was run with heat flux estimated by the equilibrium temperature method. Although simulation of currents were improved, temperature prediction was not so noticeable. To improve the temperature prediction and currents, the inverse method was used to estimate the heat flux at the water surface. Assuming the advection effect negligible, total fluxes at five stations were obtained by solving the vertically one-dimensional temperature equation coupled with momentum equations.

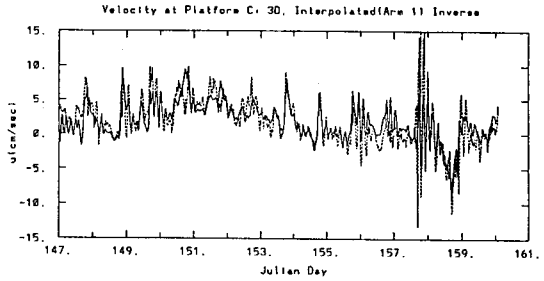

Fig. 7. Simulated (solid lines) and measured (dotted) currents (Arm 1: East-West direction). Inverse method was used for the estimation of heat flux.

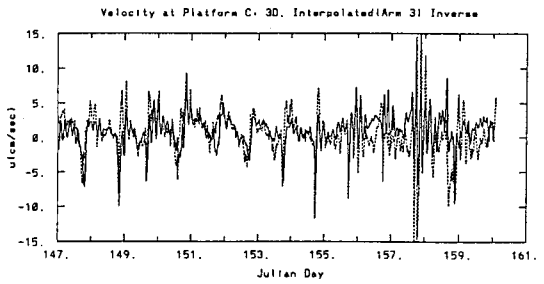

Fig. 8. Simulated (solid lines) and measured (dotted) currents (Arm 3: East-West direction). Inverse method was used for the estimation of heat flux.

Using total fluxes, CH3D was run. Trends and magnitudes of currents were similar to those with equilibrium temperature. However, temperature prediction was much improved. Figure 6 shows the temperature contour with time between Julian day 152 and 155. Generally, the lake is vertically homogeneous in the night. As sun rises, the lake becomes thermally stratified. When wind blows strong in the afternoon, the lake is destratified due to wind-induced mixing. Field data show the daily thermal stratification and destratification. The contours of simulated temperature indicate clearly this process.

Figures 7 and 8 show the simulated currents and field data. Table 3 shows the index of agreements.

As shown in Table 3, the model results with thermal effect agree well with field data. Comparing indices of Table 3 with those of Table 2, results were much improved. During the daytime, the lake becomes thermally stratified. The temperature difference between Arm 1 and Arm 3 at Station C can sometimes becomes up to 3℃. This small difference

of temperature causes the density of water to vary vertically. Although the density difference is small, the resulting buoyancy and eddy viscosity can become much different from that of homogeneous water.

Figure 7 and 8 show the time histories of temperature data and the model results. In general, the model seems to simulate the stratification well at all stations.

5. CONCLUSION

A three-dimensional hydrodynamic model (CH3 D) was significantly enhanced to study the wind-driven circulation in Lake Okeechobee considering the effects of vegetation and thermal stratification. Space- and time-varying wind stresses were used to drive the model. The effect of vegetation was parameterized as increased profile drags on the flow. Vertical turbulence was also parameterized by a simplified second order-closure model.

CH3D was used to study the wind-driven circulation during the period of May 27, 1989, to June 10, 1989, in Lake Okeechobee. Followings are major conclusions resulted from this study for Late Okeechobee.

1. It was found that thermal stratification effects were critical to the successful simulation of circulation under increasing winds.

2. Without considering thermal effects, the long-term trend of simulated currents was found to agree well with that of field data. But the simulated currents did not show the peaks well, which were quite obvious in the field data. Therefore, thermal effect in shallow lakes was considered by solving the temperature equation coupled with the momentum equations.

3. With thermal effect, the simulated currents not only revealed the peaks well but also followed field data on short-term trends quite well, indicating the proper parameterization of turbulence.

4. Another estimation of heat fluxes was tried with the so-called inverse method. Assuming that the total heat flux consists of a solar part and a nonsolar part, the nonsolar part was estimated by solving the vertically one-dimensional temperature equation. Total heat fluxes were used as a boundary condition at the water surface for the temperature equation of CH3D. Results showed that the predicted temperature agrees well with field data. Therefore, when there are insufficient meteorological data, the inverse method can be a good method to estimate the heat flux with given wind data and measured surface temperature.

ACKNOWLEDGEMENT

This research was funded by the South Florida Water Management District. Dr. Y.P. Sheng's guidance during this study is appreciated.

REFERENCES

Edinger, J.E. and Geyer, J.C., 1967. Heat exchange in the environment, *Pu. No. 65-902,* Edison Electric Institute, N.Y.

Gaspar, P., Andre, J.-C., and Lefevre, J.-M., 1990. The determination of the latent and sensible heat fluxes at the sea surface viewed as an inverse problem, *Journal of Geophysical Research,* **95**, pp. 16169-16178.

Johnson, B.J., 1982. Numerical modeling of estuarine hydrodynamics on a boundary-fitted coordinate system, Numerical Grid Generation, Elsevier Publishing Company, New York, NY, pp. 409-436.

Lee, H.K., 1993. Wind-driven circulation in Lake Okeehobee, Florida. Ph.D Dissertation, University of Florida.

Pielke, R.A., 1974. A three-dimensional numerical model of the sea breeze over south Florida, *Monthly Weather Review,* **102**, pp. 115-139.

Saville, T., 1952. Wind set-up and waves in shallow water, *Technical Memorandum No. 27,* Beach Erosion Board, Office of the Chief of Engineers, Corps of Engineers.

Sheng, Y.P., 1986. CH3D: A three-dimensional numerical model of coastal and estuarine circulation and transport in generalized curvilinear grids, *Technical Report No. 587,* Aeronautical Research Associates of Princeton, Princeton, NJ.

Sheng, Y.P., 1987. On modeling three-dimensional estuarine hydrodynamics, *Three-Dimensional Models of Marine and Estuarine Hydrodynamics* (J. Nihoul, ed.), Elsevier Oceanography Series, Elsevier, pp. 35-54.

Sokolnikoff, I.S., 1960. *Tensor Analysis,* John Wiley and Sons, New York.

Thompson, J.F., 1983. A boundary-fitted coordinate code for general two-dimensional regions with obstacles and boundary intrusions, *Technical Report E-83-8,* U.S. Army Eng. Waterways Experiment Station, Vicksburg, MS.

Willmott, C.J., 1981. On the validation of models, *Physical Geography,* 1981, pp. 184-195.